ICCFD13-2026-102

A Two-Way Coupled CFD–LPT Solver with a Hybrid PP–Ergun Momentum-Exchange Framework in Particle Sedimentation and Transport

Haorui Li*, Hong Yan*, Fuzhen Chen* and Fan Liu*
Corresponding author: yanhong@nwpu.edu.cn
* Northwestern Polytechnical University, 1 Dongxiang Road, Xi'an 710072, China.

Abstract: We present a high-performance, two-way coupled CFD–LPT framework for particle-laden flows spanning dilute suspensions and locally dense regimes. To enable large-scale simulations, the solver employs MPI-based domain decomposition and an FFT-based Poisson solver that accelerates the pressure-projection step. Interphase coupling is implemented with conservative Gaussian particle-to-grid projection and second-order grid-to-particle interpolation on a staggered grid. A PP–Ergun hybrid closure models fluid–particle momentum exchange by connecting dilute point-particle drag to dense packed-bed resistance through a smooth solids-volume-fraction weighting function.

Verification is conducted for single-sphere sedimentation and periodic FCC packed beds over $\phi = 0.15$–0.55 and $Re_{\mathrm{sup}} = 50$–1000. In the sedimentation case, the present point-particle prediction closely follows recent particle-resolved results and the experimental terminal-velocity trend at a fraction of the computational cost. In the packed-bed tests, the hybrid model reproduces the expected monotonic increase of F_d^* with ϕ and follows DNS-based FCC trends in the moderately dense range. Compared with a Gidaspow-type hard switching closure, it gives a smoother response across the dilute–dense transition. The results confirm conservative momentum exchange and numerical robustness, establishing a scalable foundation for future four-way coupled simulations of wall-bounded turbulent deposition.

Keywords: Multiphase Flow, Particle-Laden Flow, Particle-Fluid Coupling, Numerical Simulation.

1. Introduction

Particle-laden flows in wall-bounded and confined configurations often involve particles that are small compared with the macroscopic flow scales. In the wall-bounded turbulent-deposition problem that motivates this work, the carrier-flow mesh required for a DNS-quality calculation can already be close to the Kolmogorov scale, so resolving every particle surface would make the calculation prohibitively expensive, especially when long domains, many particles, or repeated parameter studies are needed. Euler–Lagrange point-particle methods therefore remain an attractive route: the carrier flow is resolved on an Eulerian grid, particles are tracked individually, and the particle–fluid interaction is represented by subgrid momentum-exchange closures [1–5]. Recent work has also made clear that the accuracy of this route depends not only on the single-particle drag law, but also on the point-force representation, undisturbed-velocity treatment, and consistency of two-way coupling on practical grids [6–11].

A central difficulty for deposition, accumulation, and other locally crowded particle-laden flows is that the local state need not remain dilute. Near-wall accumulation, particle clustering, or local blockage can move an initially dilute suspension toward a finite-solids-volume-fraction regime. A purely dilute point-particle drag closure then misses part of the hydrodynamic resistance associated with neighboring particles and pore-scale contraction. At the other limiting end, the Ergun relation provides a classical packed-bed resistance, and Wen–Yu, Gidaspow, Di Felice, and related closures are often used to connect dilute and dense gas–solid regimes [12–16]. These correlations give useful limiting behavior, but a hard switch between dilute and dense forms can introduce an artificial discontinuity, while applying a packed-bed expression too early can overestimate the drag at finite Reynolds number.

Particle-resolved simulations of fixed sphere assemblies provide a controlled way to examine this dilute-to-dense transition. Lattice-Boltzmann and PR-DNS studies have produced drag data and correlations for ordered and random arrays of spheres, including FCC configurations that isolate the effect of solids volume fraction, Reynolds number, and microstructure [17–22]. More recent fixed-array and pairwise-interaction studies show that the mean drag and force distribution depend on the averaging convention and on how the unresolved particle phase is represented [23–26]. Volume-filtered, interface-resolved, and porous-transport studies further show that finite-volume-fraction effects require careful treatment before a point-particle formulation can be applied to evolving particle layers [27–30]. What remains needed for a CFD–LPT prototype is a conservative implementation route that recovers the dilute point-particle response, approaches the packed-bed limit when particles locally accumulate, and passes through the intermediate range without a jump in model form. The verification in this paper is therefore component-level: sedimentation tests the dilute branch and interpolation procedure, while FCC fixed beds isolate the finite-ϕ transition; neither case is intended to reproduce an evolving wall-bounded deposition layer.

This work follows that route by developing a two-way coupled CFD–LPT prototype with a PP–Ergun hybrid momentum-exchange framework. The CFD module retains a DNS-oriented incompressible-flow formulation, while the particle phase remains unresolved and is coupled to the carrier flow through conservative particle-to-grid and grid-to-particle operators on a staggered grid. The dilute branch uses single-particle drag, the finite-ϕ transition range is blended smoothly, and the Ergun branch supplies an unresolved packed-bed resistance at the dense limit. The purpose is not to replace established finite-volume-fraction drag correlations with a universal formula. Rather, the goal is to build and test a conservative solver pathway that can later be extended to four-way coupling, wall-bounded turbulent deposition, and evolving locally dense particle layers [31–43].

The paper makes three contributions. First, it assembles an MPI/FFT-enabled two-way coupled CFD–LPT solver with conservative Gaussian particle-to-grid projection and second-order grid-to-particle interpolation. Second, it implements a continuous PP–Ergun momentum-exchange expression that preserves the dilute point-particle limit, recovers the dense Ergun branch, and avoids a Gidaspow-type hard switch over the chosen transition interval. Third, it verifies the prototype using a single-particle sedimentation case and FCC packed-bed drag/resistance cases over $\phi = 0.15$–0.55 and $Re_{\text{sup}} = 50$–1000, with additional field visualizations at $Re_{\text{sup}} = 1000$. The verification cases are used to identify both the numerical robustness of the present coupling route and the intermediate-regime drag correction still needed before wall-bounded deposition calculations with evolving solids concentration.

2. Methodology

2.1 Carrier phase

The carrier phase is treated as an incompressible Newtonian fluid. The velocity $\mathbf{u}_f$ and pressure p satisfy

$$\nabla \cdot \mathbf{u}_f = 0, \tag{1}$$

$$\rho_f \left(\frac{\partial \mathbf{u}_f}{\partial t} + \mathbf{u}_f \cdot \nabla \mathbf{u}_f \right) = -\nabla p + \mu_f \nabla^2 \mathbf{u}_f + \mathbf{S}_p, \tag{2}$$

where ρ_f and μ_f are the fluid density and dynamic viscosity. The term $\mathbf{S}_p$ is the particle-induced momentum source on the Eulerian grid. In the present sign convention, $\mathbf{F}_d^{(p)}$ denotes the force exerted by the fluid on particle p. The force applied to the carrier phase is therefore the projected reaction force divided by the receiving cell volume.

The discretization uses a staggered arrangement, with velocity components placed at cell faces and scalar quantities such as pressure, local solids volume fraction, number density, and averaged particle velocity placed at cell centers. This layout is also used by the particle-grid mapping operators introduced below.

2.2 Particle motion

Each particle is advanced in a Lagrangian frame. For the validation cases considered here, the particle equations are written as

$$\frac{d\mathbf{x}_p}{dt} = \mathbf{u}_p, \tag{3}$$

$$m_p \frac{d\mathbf{u}_p}{dt} = \mathbf{F}_d + V_p(\rho_p - \rho_f)\mathbf{g}, \qquad V_p = \frac{\pi d_p^3}{6}, \qquad m_p = \rho_p V_p, \tag{4}$$

where $\mathbf{x}_p$, $\mathbf{u}_p$, d_p, V_p, and m_p denote particle position, velocity, diameter, volume, and mass. The buoyancy-corrected gravitational term is retained for the sedimentation case. Particle-particle contact, lubrication, and collision models are not part of the present validation set and are left for later four-way coupling studies.

2.3 Point-particle drag

The dilute-limit force is written in the standard point-particle form. The relative velocity is

$$\mathbf{u}_{rel} = \mathbf{u}_f(\mathbf{x}_p) - \mathbf{u}_p, \tag{5}$$

and the particle Reynolds number is

$$Re_p = \frac{\rho_f |\mathbf{u}_{rel}| d_p}{\mu_f}. \tag{6}$$

The point-particle drag force is written in a Stokes-corrected form,

$$\mathbf{F}_{pp} = 3\pi \mu_f d_p C_{\mathrm{SN}}(Re_p)\mathbf{u}_{rel}. \tag{7}$$

For the present baseline implementation, C_{SN} follows the Schiller–Naumann correction in the low and moderate Reynolds-number range and a constant-drag high-Re_p branch in the equivalent Stokes-correction form:

$$C_{\mathrm{SN}} = \begin{cases} 1 + 0.15 Re_p^{0.687}, & Re_p \le 1000, \\ 0.44 Re_p/24, & Re_p > 1000. \end{cases} \tag{8}$$

The second branch of (8) is the same high-Reynolds-number drag limit that gives a classical drag coefficient of 0.44. The point-particle expression in (7) is retained without dense-phase correction when the local solids volume fraction is below the lower transition value.

2.4 Ergun resistance

The dense-limit expression is based on the Ergun packed-bed resistance [12]. The local void fraction is

$$\epsilon = 1 - \phi_s, \tag{9}$$

where ϕ_s is the solids volume fraction. In the implemented route, particle information is first mapped to the Eulerian grid. The P2G operation distributes particle volume and solid-phase momentum to cell centers, giving $\phi_{s,i}$, ϵ_i, and the local solid-phase mean velocity $\mathbf{U}_{s,i}$. The mean slip used by the Ergun branch is then

$$\mathbf{U}_{E,i} = \mathbf{u}_{f,i} - \mathbf{U}_{s,i}, \qquad U_{E,i} = |\mathbf{U}_{E,i}|. \tag{10}$$

This velocity represents the flow through the local particle assembly rather than the slip around a single isolated particle. For the static FCC arrays used in the fixed-bed validation, $\mathbf{U}_{s,i} = \mathbf{0}$. The Ergun force density on the grid is written as

$$\mathbf{f}_{E,i} = \left[150 \frac{\mu_f \phi_{s,i}^2}{\epsilon_i^3 d_p^2} + 1.75 \frac{\rho_f \phi_{s,i}}{\epsilon_i^3 d_p} U_{E,i} \right] \mathbf{U}_{E,i}. \tag{11}$$

The direction of $\mathbf{f}_{E,i}$ is therefore the direction of the mean slip. When the mean slip vanishes, the Ergun contribution vanishes as well. After the grid-level force density is obtained, the G2P operation interpolates it to particle positions and distributes the local dense-limit resistance to individual particles. With $n_{s,i}$ denoting the grid number density of particles, the corresponding single-particle Ergun force is evaluated as

$$\mathbf{F}_E^{(p)} = \epsilon_p \frac{\mathcal{I}_{g\to p}(\mathbf{f}_E)}{\mathcal{I}_{g\to p}(n_s)}, \tag{12}$$

where $\mathcal{I}_{g\to p}$ denotes the same grid-to-particle interpolation used for other cell-centered quantities. The factor $\epsilon_p = \mathcal{I}_{g\to p}(\epsilon)$ is the void fraction at the particle position. It follows the force convention used in the abstract and in the fixed-bed comparison, so that the particle-level drag excludes the pressure-gradient part of the packed-bed balance. In the FCC validation, the resulting $F_E^{(p)}$ is compared with the Ergun and Gidaspow curves plotted with the same nondimensionalization. In the hybrid force expression below, $\mathbf{F}_E$ denotes this single-particle Ergun force.

2.5 Continuous PP–Ergun drag formulation

The total drag force is written as

$$\mathbf{F}_H = (1 - w_\phi)\mathbf{F}_{pp} + w_\phi \mathbf{F}_E, \tag{13}$$

or equivalently,

$$\mathbf{F}_H = \mathbf{F}_{pp} + w_\phi(\mathbf{F}_E - \mathbf{F}_{pp}). \tag{14}$$

The weighting function w_ϕ depends on the local solids volume fraction. With

$$\phi_{low} = 0.2, \qquad \phi_{high} = 0.4, \tag{15}$$

define

$$\xi_\phi = \frac{\phi_s - \phi_{low}}{\phi_{high} - \phi_{low}}. \tag{16}$$

The clipped smoothstep function is

$$S_c(\xi) = \begin{cases} 0, & \xi \le 0, \\ 3\xi^2 - 2\xi^3, & 0 < \xi < 1, \\ 1, & \xi \ge 1. \end{cases} \tag{17}$$

The weighting function is then

$$w_\phi(\phi_s) = S_c\left(\frac{\phi_s - 0.2}{0.4 - 0.2}\right). \tag{18}$$

Therefore,

$$\phi_s \le 0.2 \Rightarrow \mathbf{F}_H = \mathbf{F}_{pp}, \qquad \phi_s \ge 0.4 \Rightarrow \mathbf{F}_H = \mathbf{F}_E. \tag{19}$$

The formulation differs from a Gidaspow-type hard switch in that the model form varies continuously through the prescribed interval. This continuity is useful for implementation and for avoiding a sudden change in the force model near a chosen threshold. At the same time, the expression is intentionally simple: it connects the point-particle and Ergun limits directly and does not include a separate Wen–Yu-type intermediate correction. This limitation is important for interpreting the FCC results at higher Reynolds numbers.

2.6 P2G/G2P mapping and coupling algorithm

The solver exchanges information between Lagrangian particles and the Eulerian grid in two directions. Figure 1 shows the overall coupling workflow, and Figure 2 shows the particle-to-grid and grid-to-particle mapping stencils.

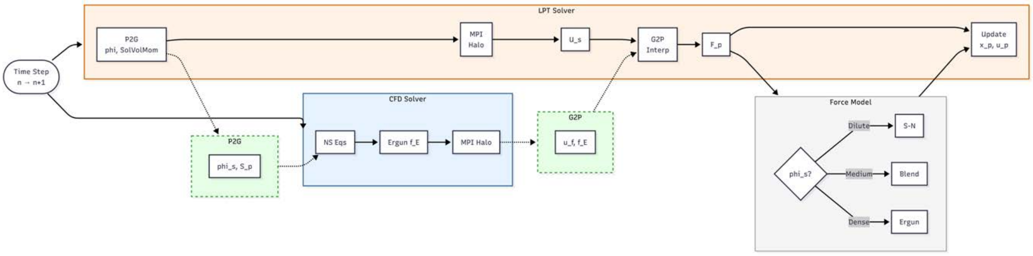

Figure 1: Two-way coupled CFD–LPT workflow. The diagram shows particle-to-grid mapping of solids fields, halo exchange, carrier-flow update, grid-to-particle interpolation, drag-force evaluation, particle update, and force projection back to the Eulerian grid.

In the first particle-to-grid step, particle volume and momentum are distributed to neighboring cell centers using a compact Gaussian kernel. For particle p and grid cell i,

$$w_i^{(p)} = \exp\left(-\frac{\|\mathbf{x}_i - \mathbf{x}_p\|^2}{2\sigma^2}\right), \qquad \widetilde{w}_i^{(p)} = \frac{w_i^{(p)}}{\sum_{j\in\mathcal{N}(p)} w_j^{(p)}}. \tag{20}$$

The local solids volume fraction, number density, and particle-phase momentum are then evaluated as

$$\phi_{s,i} = \frac{1}{\Delta V}\sum_p V_p \widetilde{w}_i^{(p)}, \tag{21}$$

$$n_{s,i} = \frac{1}{\Delta V}\sum_p \widetilde{w}_i^{(p)}, \qquad (\phi_s \mathbf{U}_s)_i = \frac{1}{\Delta V}\sum_p V_p \mathbf{u}_p \widetilde{w}_i^{(p)}. \tag{22}$$

Grid-to-particle interpolation provides the fluid velocity and cell-centered scalar fields at the particle position:

$$q(\mathbf{x}_p) = \sum_{i\in\mathcal{N}_2(p)} q_i W_i^{(p)}, \tag{23}$$

where $W_i^{(p)}$ denotes the second-order interpolation weight. After the particle force is evaluated, the reaction force is projected back to the grid using the corresponding force-distribution stencil,

$$\mathbf{S}_{p,i} = -\frac{1}{\Delta V}\sum_p \mathbf{F}_d^{(p)} W_i^{(p)}. \tag{24}$$

The force projection uses the same second-order weights as the G2P interpolation in (23). The time-step sequence is: construct particle fields on the grid, exchange halo data for mapped quantities, advance the carrier phase with the current particle source, interpolate grid quantities back to particles, evaluate the drag force, update particle motion, and project the force reaction to the grid for the next coupled step. This ordering keeps the mapped solids fraction, solid-phase mean velocity, grid force density, and single-particle force in the same P2G/G2P exchange framework.

3. Results and Discussion

3.1 Single-particle sedimentation

The single-particle sedimentation case is configured to examine the dilute side of the formulation, so the particle force is evaluated by the point-particle branch in (7). A steel sphere of diameter $d_p = 3.18{\times}10^{-3}$ m and density $\rho_p = 7820\,\mathrm{kg\,m^{-3}}$ settles in water with $\rho_f = 1000\,\mathrm{kg\,m^{-3}}$ and $\nu = 1.0\times10^{-6}\,\mathrm{m^2\,s^{-1}}$. The computational channel is $0.115\,\mathrm{m}\times0.28\,\mathrm{m}\times0.03\,\mathrm{m}$ and is discretized by a $36\times88\times10$ grid, giving a

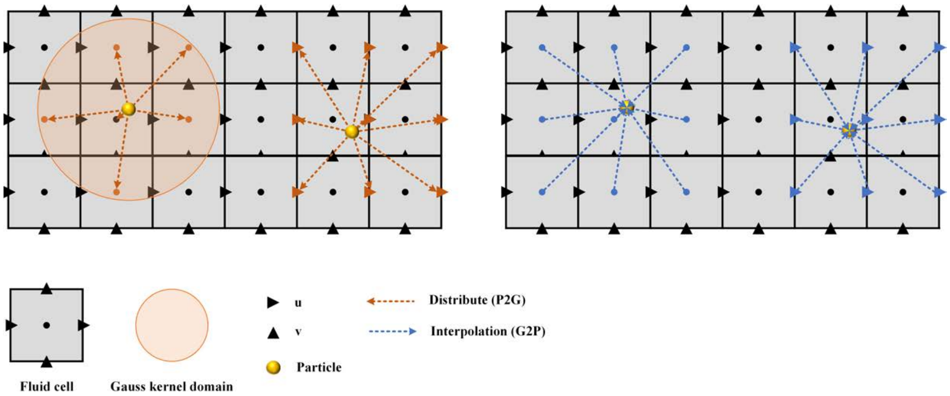

Figure 2: Particle-to-grid and grid-to-particle transfer stencils on the staggered grid. Gaussian mapping is used to construct local solids fields, while second-order interpolation is used to obtain grid quantities at particle locations and to distribute force feedback.

cell size close to the particle diameter. The particle is initially placed near the upper part of the channel and is driven by gravity in the vertical direction, while the carrier phase is initially quiescent. The lateral and spanwise directions are periodic and the two vertical boundaries are no-slip walls. The maximum time step is 1.0×10^{-4} s.

Figure 3 shows the falling velocity as a function of falling distance. The comparison includes the present result, reference data from Maya Fogouang et al. [38], an experimental terminal-velocity trend included in the comparison, and an OpenFOAM unresolved result. The present point-particle prediction closely follows the Maya Fogouang et al. reference curves over the plotted falling distance and lies within their reference envelope. During the initial acceleration stage, the slope and curvature of the velocity history are captured without an evident phase lag; at larger falling distances, the curve approaches the same terminal-velocity level indicated by the experimental comparison. In contrast, the OpenFOAM unresolved result shown in the same figure settles to a visibly higher terminal velocity. This agreement indicates that, in the dilute branch, the present G2P velocity interpolation and Schiller–Naumann force evaluation recover the reference falling-velocity trend while retaining the computational economy of a point-particle description.

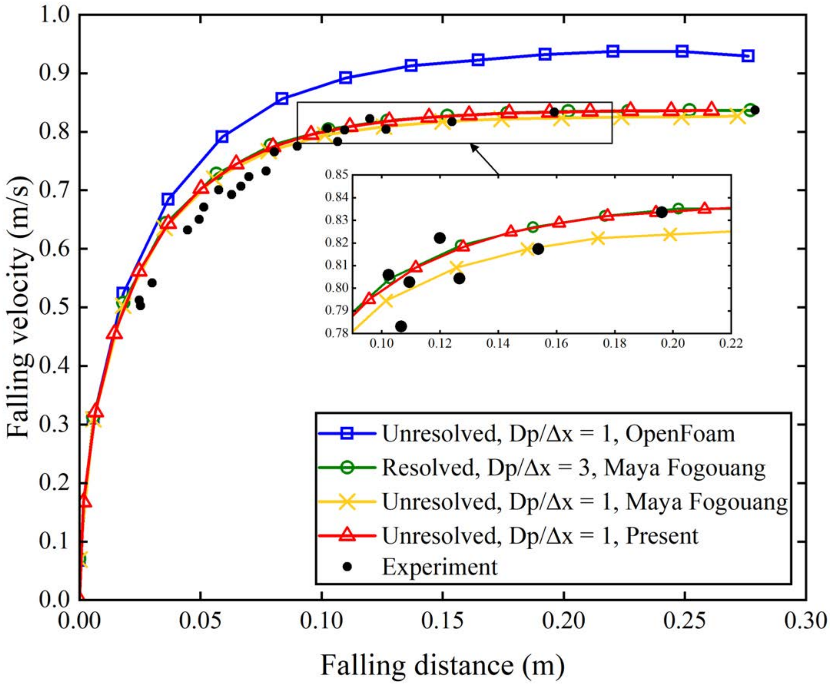

Figure 3: Single-particle sedimentation: falling velocity as a function of falling distance. The present result is compared with the Maya Fogouang et al. reference data, the experimental terminal-velocity trend included in the comparison, and an OpenFOAM unresolved result.

3.2 FCC fixed-bed drag and field structure

The FCC fixed-bed cases examine the finite-volume-fraction side of the same solver and force expression. Static monodisperse spheres are arranged in an FCC configuration. The plotted quantity is the dimensionless drag F_d^* as a function of solids volume fraction ϕ. Following the fixed-array convention, the superficial Reynolds number is

$$Re_{\text{sup}} = \epsilon Re_p, \tag{25}$$

where Re_p is based on the local interstitial velocity and $\epsilon = 1 - \phi$ is the global bed void fraction. The ensemble-averaged particle friction drag is nondimensionalized as

$$F_d^* = \frac{\left\langle F_{d,\parallel}^{(p)} \right\rangle_p}{F_{\text{St}}}, \qquad F_{\text{St}} = 3\pi\mu_f d_p U_{\text{sup}}. \tag{26}$$

Here $\left\langle F_{d,\parallel}^{(p)} \right\rangle_p$ is the ensemble-averaged particle friction drag in the mean-flow direction and U_{sup} is the superficial velocity. The superficial velocity satisfies $U_{\text{sup}} = \epsilon U_{\text{int}}$, so (25) is consistent with the interstitial-velocity definition of Re_p. The four simulated Reynolds numbers are

$$Re_{\text{sup}} = 50, \quad 200, \quad 500, \quad 1000. \tag{27}$$

The main FCC case parameters are summarized in Table 1. The solid volume fractions span the prescribed transition interval $0.2 \le \phi \le 0.4$ and extend to the denser side. The present result is compared with Ergun, Gidaspow, and Tang et al. [12, 14, 22].

Figure 4 collects the mean drag results at $Re_{\text{sup}} = 50$, 200, 500, and 1000. Across all four Reynolds numbers, the present curve varies continuously with solids volume fraction and passes through $0.2 \le \phi \le 0.4$ without a discontinuous change in model form. This behavior follows from (13): on the low-ϕ side

Table 1: Main parameters of the FCC fixed-bed cases.

Quantity	Value
Particle arrangement	Static FCC array, $6 \times 6 \times 6$ FCC cells, four spheres per FCC cell, $N_p = 864$
Particle properties	$d_p = 1.6 \times 10^{-3}$ m, $\rho_p = 500\,\mathrm{kg\,m^{-3}}$
Fluid properties	$\rho_f = 1.0\,\mathrm{kg\,m^{-3}}$, $\nu = 1.0 \times 10^{-5}\,\mathrm{m^2\,s^{-1}}$
Solid volume fractions	$\phi = 0.15$–0.55 for the drag curves; $\phi = 0.15$, 0.25, 0.35, and 0.45 for the $Re_{\mathrm{sup}} = 1000$ field slices
Reynolds numbers	$Re_{\mathrm{sup}} = 50$, 200, 500, and 1000, with $U_{\mathrm{sup}} = Re_{\mathrm{sup}}\nu/d_p$
Domain and boundaries	Periodic cubic domain, $L = (N_p \pi d_p^3/6\phi)^{1/3}$, six periodic boundaries
Grid and time advancement	$10 \times 10 \times 10$ uniform grid, third-order Runge–Kutta carrier-phase advancement, $dt_{\mathrm{max}} = 1.0 \times 10^{-5}$ s
Coupling and force model	Two-way CFD–LPT fixed-bed calculation, second-order interpolation, continuous PP–Ergun transition over $0.20 \le \phi_s \le 0.40$

the force remains close to the point-particle contribution, while on the dense side the Ergun contribution becomes dominant.

The Reynolds-number dependence is most visible in the dense part of Figure 4. At $Re_{\mathrm{sup}} = 50$, the visual comparison shows the present curve closest to the fixed-array reference trend among the four cases. As Re_{sup} increases to 200, 500, and 1000, the inertial contribution in the Ergun resistance becomes progressively stronger. Consequently, once w_ϕ gives a large contribution to the Ergun branch, the present curve can rise above the Tang et al. reference over part of the high-ϕ range. The comparison therefore supports the intended continuity of the implementation, while also showing that a direct connection between point-particle drag and packed-bed resistance is not a complete finite-volume-fraction closure at high Reynolds number.

The $Re_{\mathrm{sup}} = 1000$ field slices in Figure 5 show the streamwise velocity normalized by the superficial velocity and the mapped solids volume fraction at $\phi = 0.15$, 0.25, 0.35, and 0.45. Each row corresponds to one operating condition, with the velocity slice on the left and the mapped volume-fraction slice on the right. The superficial velocity is the same in these four cases, while the interstitial velocity increases as the void space decreases.

At $\phi = 0.15$, the represented flow field contains wider connected passages around the fixed particles and the mapped particle-centered volume-fraction regions remain relatively separated. As ϕ increases through 0.25 and 0.35, the available void space narrows and the mapped solids field occupies more of the transition interval used by (18). At $\phi = 0.45$, the high-speed regions are more localized and the mapped volume-fraction field lies predominantly on the dense side of the transition interval. These fields are consistent with the interpretation of Figure 4d that the increase in mean drag is associated with activation of the dense-limit Ergun contribution over a larger part of the particle array.

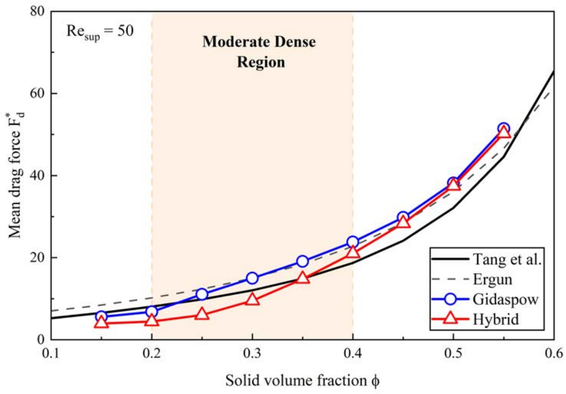

(a) Re_{sup} = 50

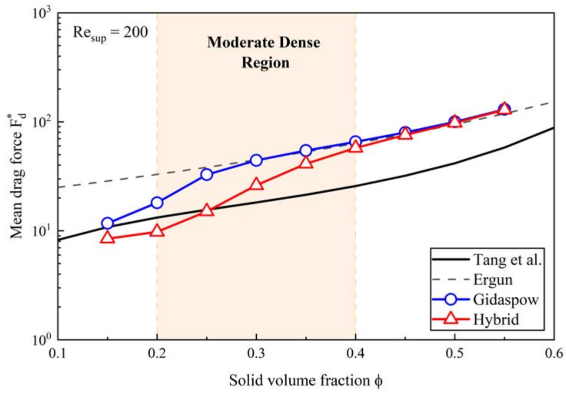

(b) Re_{sup} = 200

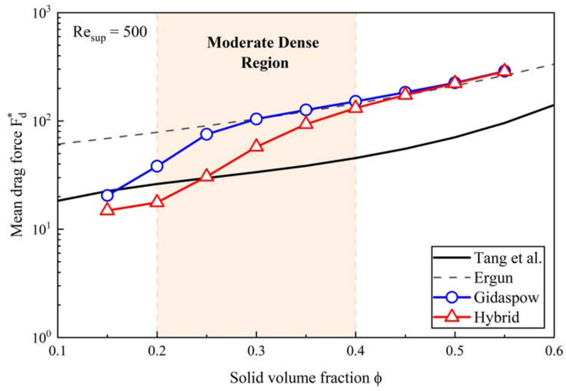

(c) Re_{sup} = 500

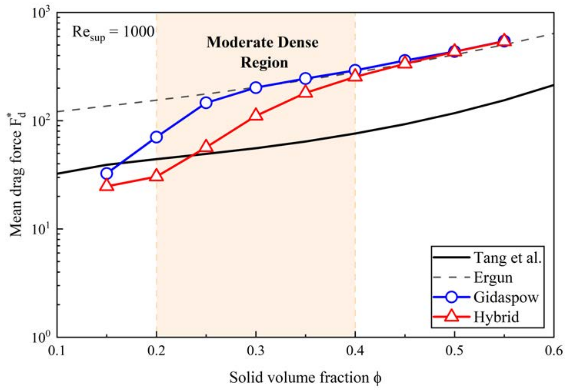

(d) Re_{sup} = 1000

Figure 4: FCC fixed-bed drag as a function of solids volume fraction. The four panels show Re_{sup} = 50, 200, 500, and 1000, respectively, with comparisons against Ergun, Gidaspow, and Tang et al.

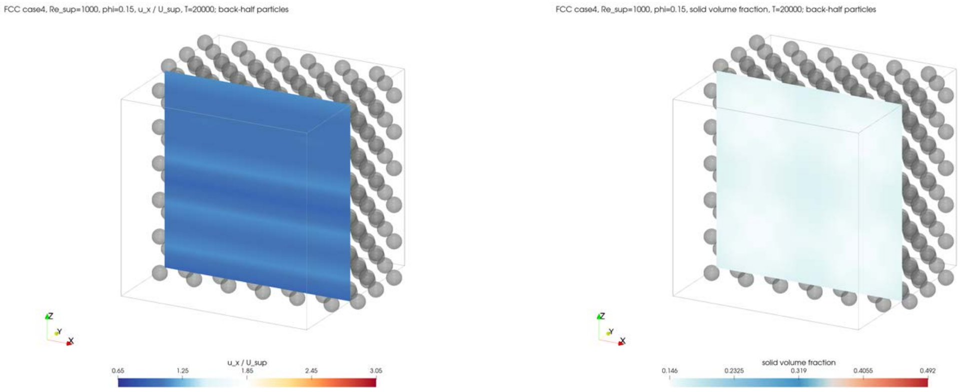

(a) $\phi = 0.15$

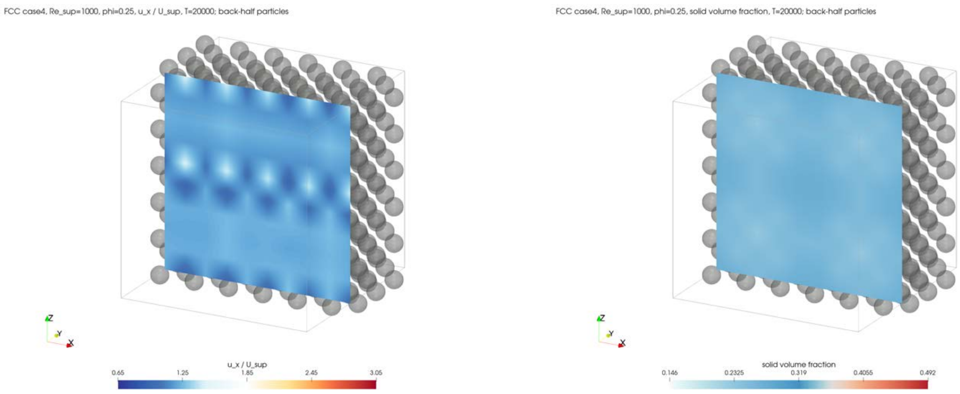

(b) $\phi = 0.25$

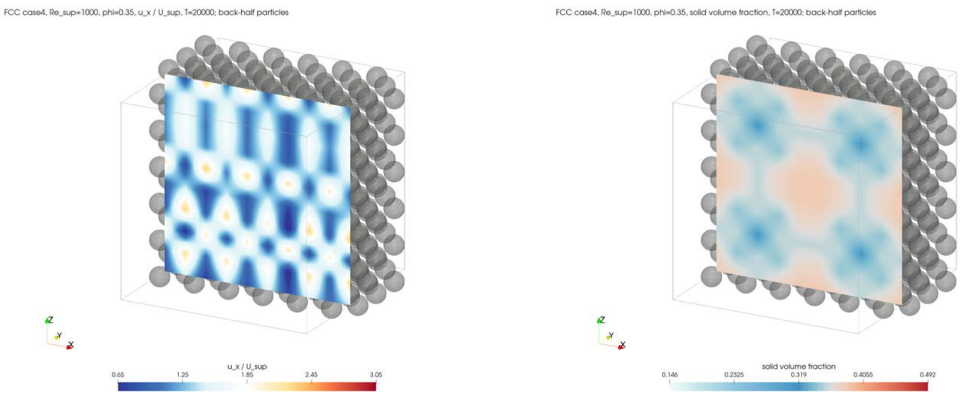

(c) $\phi = 0.35$

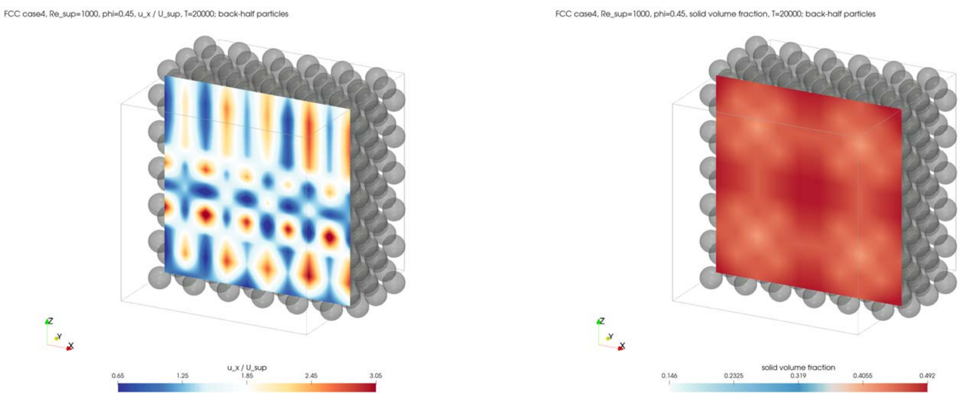

(d) $\phi = 0.45$

Figure 5: Paired field slices for the FCC fixed-bed cases at $Re_{\text{sup}} = 1000$. Each row shows one solids volume fraction at the sampled state; the left image is u_x/U_{sup} and the right image is the mapped solids volume fraction, with the same color scale used across rows for each variable.

4. Conclusions and Future Work

A two-way coupled CFD–LPT solver has been developed as a conservative numerical building block toward wall-bounded turbulent particle deposition problems in which the carrier flow can be treated with a DNS-quality formulation while the particles remain unresolved. The implementation combines MPI domain decomposition, an FFT-accelerated pressure projection, conservative particle-to-grid projection, second-order grid-to-particle interpolation, and a PP–Ergun hybrid momentum-exchange framework.

The verification cases were selected to test two limiting roles of the formulation. In single-particle sedimentation, the calculation exercises the dilute Schiller–Naumann point-particle branch. The resulting falling-velocity curve closely follows the Maya Fogouang et al. reference data and approaches the experimental terminal-velocity trend, supporting the dilute-limit particle update and interpolation procedure. The FCC fixed-bed calculations then exercise the same coupling framework at finite solids volume fraction over $Re_{\text{sup}} = 50$, 200, 500, and 1000. In these cases the mean drag varies continuously through the prescribed transition interval, while the $Re_{\text{sup}} = 1000$ field slices are consistent with the expected narrowing of represented void passages and with a larger portion of the mapped solids field lying on the dense side of the hybrid force expression.

These results also clarify the intended scope of the present closure. Within the conservative P2G/G2P coupling framework, the PP–Ergun expression provides a continuous connection between the isolated-particle response and the packed-bed resistance, which is the behavior needed for a robust two-way coupled prototype. It should not, however, be interpreted as a complete finite-volume-fraction drag law or used without further calibration for evolving wall-bounded particle layers. Because the dense branch is tied directly to the Ergun resistance, the inertial term can make the predicted drag larger than particle-resolved FCC trends at high ϕ and high Re_{sup}. A natural next refinement is therefore to introduce an intermediate finite-volume-fraction correction, guided by fixed-array or particle-resolved data, while preserving the conservative P2G/G2P transfer and the smooth transition between dilute and dense regimes.

With this boundary made explicit, the present solver provides a verification step toward the intended wall-bounded deposition problem. The carrier-flow module follows a DNS-quality incompressible-flow formulation, whereas the mesh resolution in the present validation cases is mainly set by the particle-to-grid size-ratio requirements of coarse-grained point-particle modeling rather than by a Kolmogorov-scale DNS constraint. Future work will proceed in three steps: first, introducing an intermediate finite-volume-fraction correction for the transition range; second, testing near-wall and turbulent configurations, including wall effects and undisturbed-velocity treatment; and third, extending the framework to four-way coupling with particle collisions, near-wall accumulation, evolving local solids concentration, and feedback on near-wall turbulence within the same conservative momentum-exchange framework.

Acknowledgements

This work was supported by the National Natural Science Foundation of China.

References

[1] Martin R. Maxey and James J. Riley. Equation of motion for a small rigid sphere in a nonuniform flow. *Physics of Fluids*, 26(4):883–889, 1983.
[2] S. Elghobashi. On predicting particle-laden turbulent flows. *Applied Scientific Research*, 52(4):309–329, 1994.
[3] S. Balachandar and John K. Eaton. Turbulent dispersed multiphase flow. *Annual Review of Fluid Mechanics*, 42(1):111–133, 2010.
[4] Jesse Capecelatro and Olivier Desjardins. An euler–lagrange strategy for simulating particle-laden flows. *Journal of Computational Physics*, 238:1–31, 2013.
[5] Luca Brandt and Filippo Coletti. Particle-laden turbulence: Progress and perspectives. *Annual*

Review of Fluid Mechanics, 54(1):159–189, 2022.

[6] Peter J. Ireland and Olivier Desjardins. Improving particle drag predictions in euler–lagrange simulations with two-way coupling. *Journal of Computational Physics*, 338:405–430, 2017.

[7] Fabian Evrard, Fabian Denner, and Berend van Wachem. Quantifying the errors of the particle-source-in-cell euler–lagrange method. *International Journal of Multiphase Flow*, 135:103535, 2021.

[8] Jeremy A. K. Horwitz and Ali Mani. Accurate calculation of stokes drag for point–particle tracking in two-way coupled flows. *Journal of Fluid Mechanics*, 931:A3, 2021.

[9] Pedram Pakseresht, Mahdi Esmaily, and Sourabh V. Apte. A correction scheme for two-way coupled point-particle simulations on anisotropic grids. *Journal of Computational Physics*, 439:110381, 2021.

[10] Praneeth Chandran, Jessica L. Kozarek, Sourabh V. Apte, and Marshall C. Richmond. A correction scheme for point-particle models applied to a non-linear drag law in simulations of particle-laden flows. *Journal of Computational Physics*, 520:113496, 2025.

[11] Berend van Wachem, Michael Hausmann, Fabian Evrard, and Fabian Denner. A unified paradigm to derive mathematical models for particle-laden flows. *Journal of Fluid Mechanics*, 1018:A6, 2025.

[12] Sabri Ergun. Fluid flow through packed columns. *Chemical Engineering Progress*, 48(2):89–94, 1952.

[13] C. Y. Wen and Y. H. Yu. Mechanics of fluidization. In *Chemical Engineering Progress Symposium Series*, volume 62 of *62*, pages 100–111, 1966.

[14] Dimitri Gidaspow. *Multiphase Flow and Fluidization: Continuum and Kinetic Theory Descriptions*. Academic Press, 1994.

[15] R. Di Felice. The voidage function for fluid–particle interaction systems. *International Journal of Multiphase Flow*, 20(1):153–159, 1994.

[16] Y. Tsuji, T. Kawaguchi, and T. Tanaka. Discrete particle simulation of two-dimensional fluidized bed. *Powder Technology*, 77(1):79–87, 1993.

[17] Anthony J. C. Ladd. Numerical simulations of particulate suspensions via a discretized boltzmann equation. part 1. theoretical foundation. *Journal of Fluid Mechanics*, 271:285–309, 1994.

[18] Robert J. Hill, Donald L. Koch, and Anthony J. C. Ladd. The first effects of fluid inertia on flows in ordered and random arrays of spheres. *Journal of Fluid Mechanics*, 448:243–278, 2001.

[19] R. Beetstra, M. A. van der Hoef, and J. A. M. Kuipers. Drag force of intermediate reynolds number flow past mono- and bidisperse arrays of spheres. *AIChE Journal*, 53(2):489–501, 2007.

[20] Sudheer Tenneti, Rahul Garg, and Shankar Subramaniam. Drag law for monodisperse gas–solid systems using particle-resolved direct numerical simulation of flow past fixed assemblies of spheres. *International Journal of Multiphase Flow*, 37(9):1072–1092, 2011.

[21] Sudheer Tenneti and Shankar Subramaniam. Particle-resolved direct numerical simulation for gas–solid flow model development. *Annual Review of Fluid Mechanics*, 46(1):199–230, 2014.

[22] Yali Tang, E. A. J. F. Peters, J. A. M. Kuipers, S. H. L. Kriebitzsch, and M. A. van der Hoef. Flow past monodisperse static arrays of spheres. *AIChE Journal*, 61(2):688–698, 2015.

[23] Georges Akiki, Thomas L. Jackson, and S. Balachandar. Force variation within arrays of monodisperse spherical particles. *Journal of Fluid Mechanics*, 813:882–928, 2017.

[24] Georges Akiki, Will Moore, and S. Balachandar. Pairwise interaction extended point-particle model for a random array of monodisperse spheres. *Journal of Computational Physics*, 351:329–357, 2017.

[25] Mohammad Mehrabadi, Sudheer Tenneti, Rahul Garg, and Shankar Subramaniam. Pseudo-turbulent gas-phase velocity fluctuations in homogeneous gas–solid flow: Fixed particle assemblies and freely evolving suspensions. *Journal of Fluid Mechanics*, 850:336–369, 2018.

[26] Joao Pedro Vila, Fabio H. Hayashi, Julian C. Santos, Oswaldo A. Z. Sotomayor, and Dirceu Noriler. Gas flow through static particle arrangements with a channel: Resolved simulations and analytic considerations. *Chemical Engineering Science: X*, 2:100015, 2019.

[27] Michael Hausmann, Fabian Denner, Fabian Evrard, and Berend van Wachem. Study and derivation of closures in the volume-filtered framework for particle-laden flows. *Journal of Fluid Mechanics*,

996:A18, 2024.

[28] Berend van Wachem, Jasper Pas, Stefano Sibilla, and Fabian Denner. Discrete formulation and consistent linearization of the volume-filtered euler–lagrange equations for particle-laden flows. *International Journal of Multiphase Flow*, 175:104815, 2024.

[29] Yonghui Xia, Youcheng Jiang, Shenghong Liang, Bo Sun, Jian Zhu, and Kun Luo. Modelling of filtered drag force for clustered particle-laden flows based on interface-resolved simulation data. *Journal of Fluid Mechanics*, 998:A2, 2024.

[30] Filip Sadowski, S. Balachandar, and David H. Richter. Interaction history model for particle clusters in particle-laden flows. *Physics of Fluids*, 36(2):023307, 2024.

[31] P. Gualtieri, F. Picano, G. Sardina, and C. M. Casciola. Exact regularized point particle method for multiphase flows in the two-way coupling regime. *Journal of Fluid Mechanics*, 773:520–561, 2015.

[32] Francesco Battista, Jean-Philippe Mollicone, Paolo Gualtieri, Roberto Messina, and Carlo Massimo Casciola. Exact regularised point particle method (erpp) for particle-laden wall-bounded flows in the two-way coupling regime. *International Journal of Multiphase Flow*, 101:113–124, 2018.

[33] Jean-Francois Poustis, Jean-Michel Senoner, Stephane Jaouen, and Jacques Magnaudet. Regularization of the lagrangian point force approximation for deterministic discrete particle simulations. *International Journal of Multiphase Flow*, 117:138–152, 2019.

[34] Francesco Battista, Jean-Philippe Mollicone, and Paolo Gualtieri. A numerical study on the effects of the undisturbed fluid velocity reconstruction on particle-laden flows in the two-way coupling regime. *Physics of Fluids*, 35(4):043324, 2023.

[35] P. Gualtieri, F. Battista, F. Salvadore, and C. M. Casciola. Effect of particle-to-fluid heat transfer on turbulence in particle-laden flows. *Journal of Fluid Mechanics*, 974:A37, 2023.

[36] Yanxing Gong, Haochao Wang, Lei Wang, and Dapeng Sun. Cp3d: A comprehensive euler–lagrange solver for direct numerical simulation of particle-laden flows. *Computer Physics Communications*, 286:108666, 2023.

[37] Laurez Maya Fogouang, Laurent Andre, and Cyprien Soulaine. Particulate transport in porous media at pore-scale. part 2: Cfd–dem and colloidal forces. *Journal of Computational Physics*, 519:113439, 2024.

[38] Laurez Maya Fogouang, Laurent Andre, and Cyprien Soulaine. Particulate transport in porous media at pore-scale. part 1: Unresolved-resolved four-way coupling cfd–dem. *Journal of Computational Physics*, 521:113540, 2025.

[39] S. T. W. Kuruneru, E. Sauret, S. C. Saha, and Y. T. Gu. A comparative study of mixed resolved-unresolved cfd–dem and unresolved cfd–dem methods for the solution of particle-laden liquid flows. *Archives of Computational Methods in Engineering*, 26(4):1239–1254, 2018.

[40] Rahul Jaiswal, Mehran Kiani-Oshtorjani, and Ali Mani. A volume-filtered euler–lagrange method for particle-laden flows. *Fluids*, 7(10):337, 2022.

[41] Q. Zhao, Q. Hou, and A. Yu. Eulerian–lagrangian modeling of dense particulate flows. *Archives of Computational Methods in Engineering*, 31(2):871–918, 2023.

[42] H. Xiao and J. Sun. Algorithms in a robust hybrid cfd–dem solver for particle-laden flows. *Communications in Computational Physics*, 9(2):297–323, 2011.

[43] Rui Sun and Hong Xiao. Diffusion-based coarse graining in hybrid continuum–discrete solvers: Applications in cfd–dem. *International Journal of Multiphase Flow*, 77:142–157, 2015.